Revista Mexicana de Astronomía y Astrofísica, 61, 35-51, (2025)

OPEN ACCESS https://doi.org/10.22201/ia.01851101p.2025.61.02.04

Investigating Open Cluster KING 6: Detection of Three New Variables

Vaibhav Kumar Pandey[1], Arvind K. Dattatrey[2], Apara Tripathi[1], R. K. S. Yadav[2] and Shantanu Rastogi[1]

[1]*Deen Dayal Upadhyaya Gorakhpur University, Gorakhpur, Uttar Pradesh, India, 273009.*
[2]*Aryabhatta Research Institute of Observational Sciences, Manora Peak, Nainital, Uttarakhand,India, 263001.*

Keywords: *clusters, photometric, stars, variables*

Abstract

This study presents a photometric analysis of the intermediate-age open cluster King 6, utilizing photometric data in $UBV(RI)_c$ passbands and JHK_s from the $2MASS$ mission. Gaia DR3 kinematic data were used to estimate the membership probabilities, and $TESS$ data were employed to search for variable stars within the cluster. The cluster's radius is estimated to be 9′.0 based on the stellar density profile, while optical and near-infrared color-color diagrams revealed color excesses of $E(B-V) = 0.58 \pm 0.03$, $E(J-K) = 0.24 \pm 0.03$, and $E(V-K) = 1.53 \pm 0.01$ mag. The interstellar extinction law is normal in the direction of the cluster. The cluster's estimated age is ∼ 251 Myr and the distance is 724 ± 5 pc. The mass function slope was found to be $x = 0.57 \pm 0.28$ by considering stars ≥ 1 $M_\odot$. Our analysis indicates that the cluster was dynamically relaxed. Furthermore, we identified three new variable stars for the first time in the cluster region using $TESS$ data. These variables belong to the category of slow-pulsating B-type variables with periods of 46.70, 47.92, and 37.56 h.

Resumen

Se presenta el análisis fotométrico del cúmulo abierto de edad-intermedia King 6, utilizando datos en las bandas fotométricas $UBV(RI)_c$ y JHK_s del censo $2MASS$. De los datos cinemáticos de Gaia DR3 se estimaron las probabilidades de pertenencia al cúmulo y los datos de $TESS$ se utilizaron para una búsqeda de estrellas variables en el cúmulo. El radio estimado del cúmulo es 9′.0 obtenido a partir del perfil de densidad estelar. Los colores en el infrarrojo cercano revelan los excesos de color $E(B-V) = 0.58 \pm 0.03$, $E(J-K) = 0.24 \pm 0.03$, y $E(V-K) = 1.53 \pm 0.01$ mag. La ley de extinción interestelar es la normal en la dirección del cúmulo. La edad del cúmulo es ∼ 251 Myr y la distancia es de 724 ± 5 pc. La pendiente de la función de masa resulta $x = 0.57 \pm 0.28$ considerando estrellas de masa ≥ 1 $M_\odot$. Nuestro análisis indica que el cúmulo está relajado dinámicamente. Finalmente, se identificaron tres nuevas estrellas variables en la región del cúmulo utilizando datos de $TESS$. Estas estrellas son variables pulsantes lentas tipo-B con períodos de 46.70, 47.92, and 37.56 hr.

Corresponding author: Apara Tripathi *E-mail address:* apara.phy@ddugu.ac.in
Received: January 3, 2025 **Accepted:** April 7, 2025

1. General

Open star clusters serve as excellent laboratories for exploring stellar evolution and dynamics in our galaxy. They provide insights into star formation processes, thereby enhancing our understanding of the universe (Lada & Lada, 2003). Open clusters (OCs) consist of stars with similar physical properties that form simultaneously from the collapse of molecular clouds (McKee & Ostriker, 2007). Although member stars share the same age, distance, and chemical composition, their masses vary (Joshi et al., 2020a). The study of OCs using astrometric and photometric observations allows us to determine the parameters of single stars (Dias et al., 2021), partially explaining the interest in these systems. Furthermore, combining astrophysical parameters, such as distance, metallicity, and age, with the kinematic properties of stars within OCs makes them valuable tools for studying the formation and evolution of the Galactic disc (Cantat-Gaudin et al., 2020). A comprehensive photometric study based on membership determination using proper motions (PMs) and parallaxes helps to understand the stellar and dynamical evolution of clusters (Tripathi et al., 2023).

King 6 is positioned at (α_{J2000} = 03:27:55.7, δ_{J2000} = +56:26:38) corresponding to Galactic coordinates l ∼ 143°.36 and b ∼ -0°.07. Trumpler (1930) classified this cluster as II2m based on V-band images. Ruprecht (1966) reclassified it in class IV2p. Ann et al. (2002), using $UBVI_c$ CCD photometry, reported mean reddening $E(B-V)$ = 0.50 ± 0.10 mag, log(age) = 8.40 ± 0.10 and distance modulus as $(m-M)_0$ = 9.70 ± 0.40 mag. Maciejewski

& Niedzielski (2007) performed a survey in BV wide-field CCD photometry. They estimated the core radius of King 6 as $3'.60 \pm 0'.40$, a log(age) value of 8.40, a distance modulus of 11.17 ± 0.51 mag, and a reddening value of 0.53 ± 0.12 mag. These parameters indicate the absence of mass segregation within the cluster. Piskunov et al. (2008) found that this cluster is poorly populated. Bossini et al. (2019) catalogued the age and fundamental parameters of 269 open clusters using data from Gaia DR2 and reported log(age) $= 8.58 \pm 0.12$, distance modulus 9.54 ± 0.02, and $A_V = 1.06 \pm 0.03$ for King 6. Gokmen et al. (2023) reported the analysis of King 6 using CCD UBV and Gaia DR3 data. They estimated the color excess, $E(B-V)$, to be 0.55 ± 0.03 mag and determined the distance as 723 ± 34 pc, with an age of 200 ± 20 Myr. The mass function slope was found to be 1.29 ± 0.18. Their analysis indicated that the cluster was dynamically relaxed. Table 5 provides a comparative overview of the parameters we derived alongside previously reported values.

There are differences in the parameter values derived for the cluster in the literature, as shown in Table 5. Previous studies on the membership of King 6 did not provide reliable estimates of the cluster members. With the availability of astrometric data from Gaia DR3 and new optical and 2MASS near-infrared datasets, we revisited OC King 6 to study its parameters and dynamical status. Additionally, the extracted parameters of the cluster will be used to enhance the sample of clusters needed for studying Galactic structure and dynamics.

The detection of variable stars provides valuable information for constraining stellar pulsation models and refining theoretical models that predict the characteristics of stars in clusters. Pulsating stars, in particular, offer insights into the internal stellar structure and mass. Intermediate-age clusters serve as excellent laboratories for studying short-period variables (Joshi et al., 2020b). Recent work on the Pleiades cluster (Bedding et al., 2020) demonstrates the power of combining observations with Gaia (Gaia Collaboration et al., 2016) and *TESS* (Transiting Exoplanet Survey Satellite) for studying pulsating stars in OCs. The large pulsational frequency separation and frequency at maximum power can help constrain stellar evolution, structure, and oscillation models, leading to a better characterization of pulsating stars. These advancements have encouraged us to use space-based data to characterize the variables in OCs. In this study, we present the results of our search for variable stars using observational data from the *TESS* mission for King 6 and report their classifications.

The remainder of this paper is structured as follows: § 2 presents the observations and data reduction. Section 3 discusses the archival data used in this analysis. In § 4, 5, 6, and 7, we discuss the cluster parameters. In § 8, we discuss the luminosity and mass function of the cluster, followed by mass segregation, relaxation time, and tidal radius in § 9.

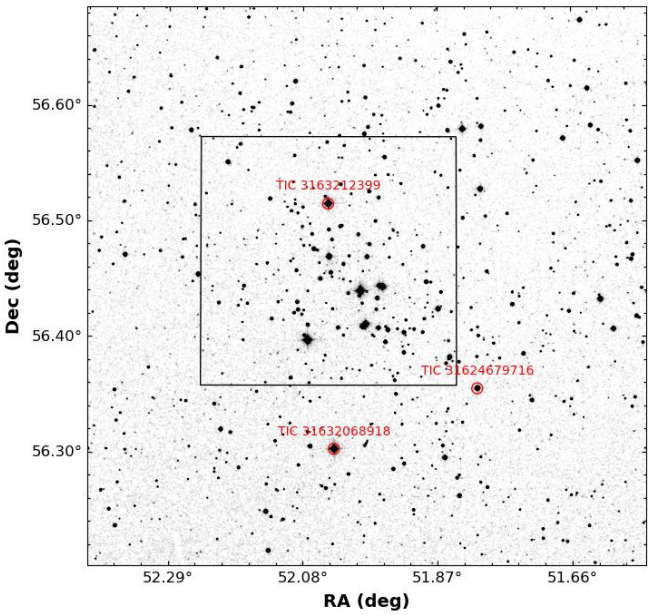

Figure 1. Identification chart for the cluster King 6, taken from SDSS. Rectangular box outlines observed region, while the red circles highlight position of variable stars.

§ 10 presents the identification of the variable stars in King 6. Finally, our work is summarized in § 11.

2. Observations and data Reduction

2.1. *UBVRI* photometric observations

This study utilized data collected with the 104-cm Sampurnanand telescope at the Aryabhatta Research Institute of Observational Sciences (ARIES) in Nainital, India. The observations were conducted from December 23^{rd} to 25^{th}, 2005. The telescope captured images in multiple bands: $UBV(IR)_C$, using a thinned back-illuminated CCD camera mounted at the f/13 Cassegrain focus. Figure 1 presents the finding chart of the cluster, which was obtained from the Sloan Digital Sky Survey (SDSS) data. The rectangular box indicates the region observed using the 104-cm Sampurnanand telescope at Manora Peak, ARIES, Nainital.

The CCD detector has pixels measuring 24 μm each, arranged in a 2048×2048 grid, providing a field of view on the sky of approximately $13' \times 13'$, with a pixel resolution of $0''.38$. A binning mode of 2×2 pixels was employed during the observations to enhance the signal-to-noise ratio. The CCD had a readout noise of 5.3 e^- and a gain factor of 10 e^-/ADU. The Observational log is shown in Table 1.

Bias and twilight flat-field frames were used for image cleaning. Multiple short and long exposures were collected for the cluster and standard fields using all filters. Calibrating the stellar magnitudes involved observing stars in the standard field PG1047+003. Several Landolt (1992) standard stars were identified within the observed field of

Table 1. Description of the optical observation for King 6 and the standard field

Cluster/ standard field	Date	Filter	Exp. time × no.of frames
King 6	$23/24^{th}$ Dec 2005	V	900×3, 120×1
		B	240×2, 1200×3
		I	60×1, 40×1
			100×2, 240×2
		R	480×3, 60×1
		U	300×2, 1800×2
PG1047+003	25^{th} Dec 2005	V	120×4, 100×1
		B	200×5
		I	60×5
		R	60×5
		U	300×5

view of PG1047+003. The IRAF data reduction package was used for the pre-processing of data frames, which includes bias subtraction, flat fielding, and cosmic ray removal. This process ensures that the data is clean for further analysis.

2.2. Photometric and astrometric calibration

Photometry on the bias-subtracted and flat-field-corrected CCD frames was performed using DAOPHOT-II software (Stetson, 1987, 2000). Quantitative values for the brightness of stars were obtained using aperture and profile-fitting photometry. The measurements of bright stars that were saturated in deep exposure frames were obtained from short-exposure frames. Least-squares linear regressions were fitted to translate the observed aperture magnitudes into standard magnitudes. The equations for calibrating the instrumental magnitudes are as follows:

$$v = V + 4.15 \pm 0.005 \text{ - } (0.002 \pm 0.004)(B - V) + (0.23 \pm 0.02)X$$

$$b = B + 4.57 \pm 0.008 \text{ - } (0.005 \pm 0.005)(B - V) + (0.38 \pm 0.02)X$$

$$i = I + 4.62 \pm 0.010 \text{ - } (0.020 \pm 0.01)(V - I) + (0.10 \pm 0.02)X$$

$$r = R + 4.08 \pm 0.006 \text{ - } (0.010 \pm 0.004)(V - R) + (0.16 \pm 0.01)X$$

$$u = U + 6.79 \pm 0.030 \text{ - } (0.006 \pm 0.01)(U - B) + (0.60 \pm 0.08)X$$

Here, V, B, I, R, and U represent standard magnitudes, and v, b, i, r, u refer to instrumental aperture magnitudes normalized for 1 s of exposure time, and X is the airmass. The zero points for the local standards were evaluated by considering the aperture growth curve, exposure time differences, and atmospheric extinction. The errors associated with the zero points and color coefficients were ~ 0.01 magnitudes.

Table 2. Description of observed errors in different filters with V magnitude bins

V range	σ_V	σ_B	σ_I	σ_R	σ_U
12-13	0.01	0.01	0.01	0.01	0.01
13-14	0.01	0.01	0.01	0.01	0.02
14-15	0.01	0.01	0.01	0.01	0.02
15-16	0.01	0.01	0.01	0.01	0.04
16-17	0.01	0.02	0.03	0.01	0.10
17-18	0.01	0.03	0.03	0.01	0.20
18-19	0.01	0.04	0.03	0.01	0.40
19-20	0.01	0.10	0.04	0.01	0.50

The internal errors calculated using DAOPHOT are plotted against V magnitudes for the $UBVRI$ filters, as shown in Figure 2. It shows an average photometric error ≤ 0.04 mag across all filters up to a V magnitude of 17. For magnitudes 17 to 20 mag, uncertainty is ~ 0.10 mag whereas for U it is ~ 0.05. Table 2 shows the error trends across the filters relative to V magnitude.

Astrometric solutions were used to obtain the celestial coordinates of all stars in $J2000.0$. We used the $CCMAP$ and $CCTRAN$ tasks of $IRAF$ to obtain the celestial coordinates of the detected stars. The sources detected in different wavebands were merged using a matching radius of $\sim 2''$. A total of 3028 stars were detected in all five survey bands in this study.

2.3. Comparison with the previous photometry

CCD $UBVI$ photometry was previously performed by Ann et al. (2002). To verify our photometry, we cross-identified the stars with the photometry of Ann et al. (2002), which yielded 158 matched sources. We estimated the difference in magnitude and plotted it against V magnitude, as shown in Figure 3. The mean of the differences and standard deviation (i.e mean $\pm \sigma$) for V, B, I_c and U magnitude is found to be 0.02 ± 0.09, 0.01 ± 0.09, -0.05 ± 0.05, and 0.04 ± 0.64 mag, respectively.

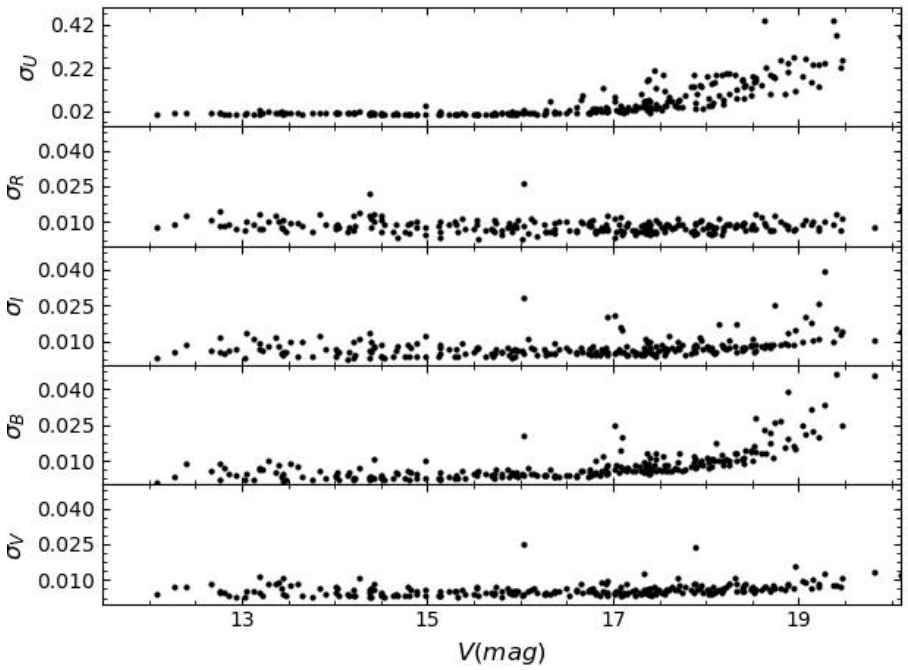

Figure 2. Photometric errors in V, B, I, R, and U against V-band magnitude. Errors on the Y-axis represent the internal error as estimated by the DAOPHOT routine.

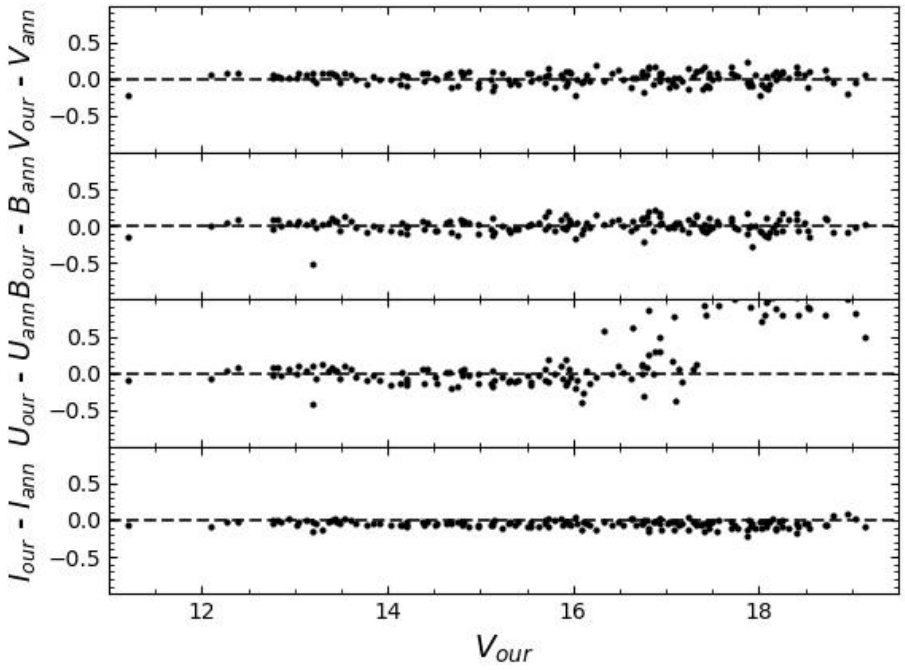

Figure 3. Comparison of the present photometry with Ann et al. (2002) in U, B, V and I_c filters against V magnitude. The dotted lines are plotted at zero value.

3. Archival Data

3.1. Gaia DR3

Gaia DR3 data were used for astrometric studies and to determine the cluster structural parameters. It provides celestial positions and G band magnitudes for a vast dataset of approximately 1.8 billion sources, with magnitude measurements extending up to 21 mag. Additionally, Gaia DR3 provides valuable parallax, proper motion, and color information ($G_{BP} - G_{RP}$) for a subset of this dataset, specifically 1.5 billion sources. The uncertainties in the parallax values are $\sim$ 0.02–0.03 milli-arcsecond (mas) for sources at $G \leq 15$ mag and $\sim$ 0.07 mas for sources with $G \sim 17$ mag. We collected data for King 6 within a radius of

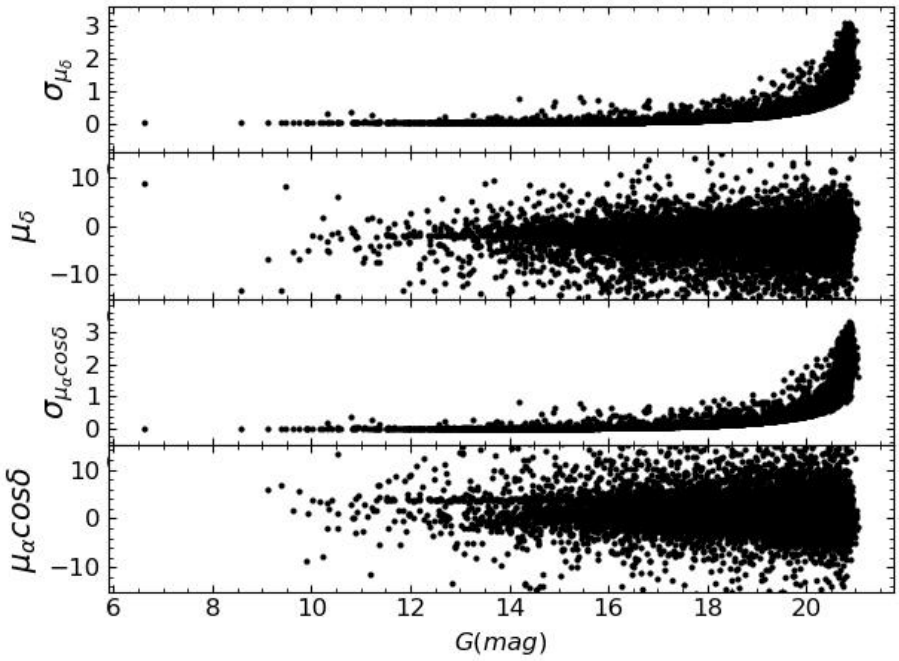

Figure 4. Proper motions in the direction of RA and DEC and its error are plotted against G mag.

Table 3. Description of uncertainties in proper motions and magnitudes against Gaia G magnitude bins

G(mag)	$\sigma_{\mu_\alpha cos\delta}$	σ_{μ_δ}	σ_G	$\sigma_{G_{RP}}$	$\sigma_{G_{BP}}$
11-12	0.020	0.020	0.002	0.003	0.004
12-13	0.020	0.020	0.002	0.003	0.004
13-14	0.030	0.030	0.002	0.004	0.004
14-15	0.040	0.040	0.003	0.005	0.005
15-16	0.050	0.050	0.003	0.006	0.005
16-17	0.070	0.070	0.003	0.010	0.005
17-18	0.114	0.110	0.003	0.030	0.007
18-19	0.198	0.196	0.004	0.070	0.013
19-20	0.384	0.385	0.005	0.120	0.024

30′. The proper motions of the stars in the cluster and the corresponding errors are graphically represented against G magnitude in Figure 4. The lower panel displays two prominent structures: uncertainties in the corresponding proper motion components are less than 0.04 mas up to 15^{th} magnitudes; ≤ 0.10 mas from 15^{th} to 18^{th} mag and less than 0.40 mas up to 20^{th} magnitudes. A detailed analysis of the uncertainties in the proper motion along the Right Ascension (RA), declination (DEC), and Gaia magnitudes (G, G_{BP}, G_{RP}) is shown in Table 3.

3.2. The Near-infrared Data

We used archival near-infrared photometric data from the Two Micron All-Sky Survey (2MASS Skrutskie et al., 2006), which provides photometry in the J (1.25 μm), H (1.65 μm), and K_s (2.17 μm) filters. The data have limiting magnitudes of 15.80, 15.10, and 14.30 in the J, H, and K_s bands, respectively, with a signal-to-noise ratio (S/N) greater than 10. Our optical data were cross-correlated with the 2MASS photometric catalogue, resulting in the identification of 233 common stars within a matching radius of 2″.

3.3. TESS (Transiting Exoplanet Survey Satellite) data

We utilized *TESS* data, which features a large plate scale of 21″ per pixel, for the analysis. This resolution often causes TESS light curves to capture the combined light from multiple stars (Higgins & Bell, 2023). In our investigation of the variable stars in our cluster, we identified three isolated stars after matching the *TESS* data with optical observations.

4. Structural Parameter of the cluster: Cluster extent

The size of a star cluster plays a crucial role in studying its dynamic evolution, which involves how the cluster changes over time owing to internal and external forces. However, determining the precise size of a cluster can be challenging because of its irregular shape, making it difficult to pinpoint the exact center and outer boundaries of the cluster. We employed a histogram-based technique to estimate the cluster center. We plotted the number of stars against their celestial coordinates (RA and DEC), as shown in Figure 5. The data for this analysis were obtained from Gaia DR3, specifically for stars with a G-band magnitude uncertainty ≤ 0.10 magnitudes and located within a 30′.0 radius of the cluster center listed in Table 5. Our analysis reveals a cluster center at approximately (03:27:55.26, +56:26:39.07)

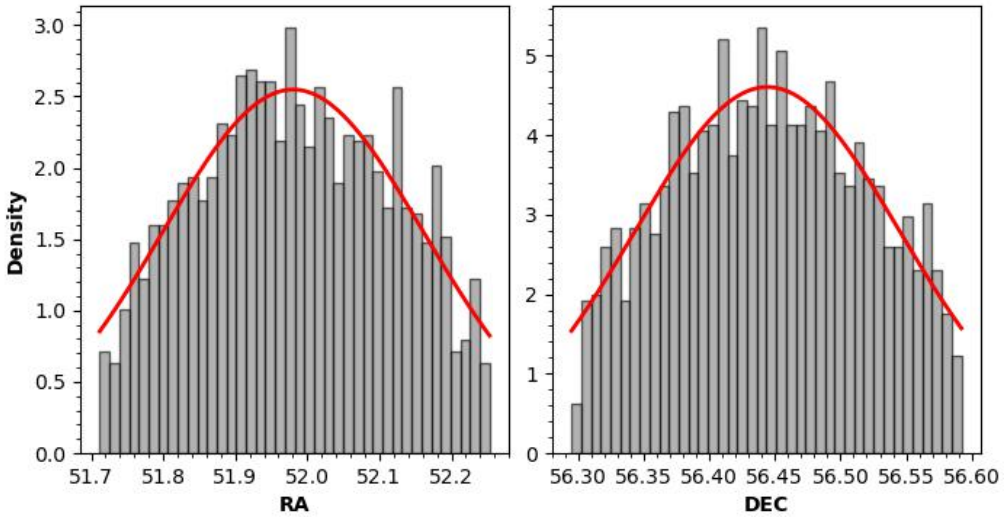

Figure 5. Histogram in RA and DEC of the stars. Solid red line represents the fitted Gaussian function.

for King 6, which is roughly 15′′.0 away from the center estimated by Ann et al. (2002).

Thus, defining the cluster radius, which indicates the point at which the internal gravitational influence becomes negligible, is crucial. We achieved this by analyzing the stellar density profile. To conduct a quantitative analysis, we created concentric annular regions (ring-shaped areas) around the estimated cluster center. We then counted the number of stars within each annular ring (width of 0′.50) and divided this count by the corresponding area of the ring to calculate the number density of stars in that region. This method allowed us to examine how the density of stars varied with distance from the cluster center, ultimately helping us determine the effective radius of the cluster. To estimate this radius, we fitted the surface density profile described by King (1962) to the stellar radial distribution. This fit was accomplished using a nonlinear least-squares routine that considered the errors as weighting factors. The radial density profile (RDP) is represented as follows:

$$\rho(r) = \frac{\rho_0}{1 + (\frac{r}{r_c})^2} + \rho_b \quad (1)$$

where ρ_0 is the central density, r_c is the core radius of the cluster, and ρ_b is the background density.

Figure 6 illustrates the best-fit solution for the density distribution of King 6, along with its associated uncertainties. As is evident from the graphs, the radial density profile for the clusters exhibits a decline, followed by a flattening behavior at approximately 9′.0. Based on this observation, we adopted 9′.0 as the cluster radius, which is slightly lower than the values previously reported by Maciejewski & Niedzielski (2007) and Gokmen et al. (2023), as shown in Table 5. For King 6, $\rho_0 = 5.88$ stars arcmin^{-2}, $r_c = 3.58$ arcmin and $\rho_b = 7.00$ stars/arcmin^2.

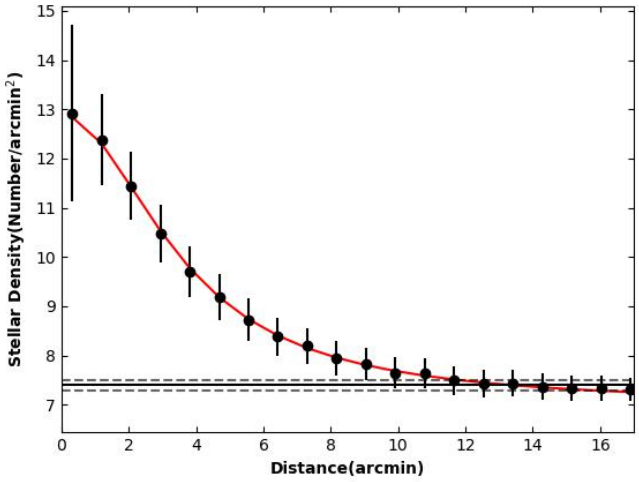

Figure 6. Radial density profile of the cluster King 6. The red solid curve represents the best fit of King (1962). Solid horizontal line represents the background density, wheras dashed lines represent the errors.

The value of the core radius r_c is comparable within error to the values reported by Gokmen et al. (2023) (see Table 5).

5. Determination of membership probability

A significant challenge in studying OCs is the presence of unrelated stars along the line of sight, known as field star contamination. Distinguishing these field stars from the actual members of the cluster is crucial for accurately estimating the cluster's physical and dynamical properties (Angelo et al., 2019, 2020). An effective method for separating members from field stars is the vector point diagram (VPD) based on proper motion (Dias et al., 2018).

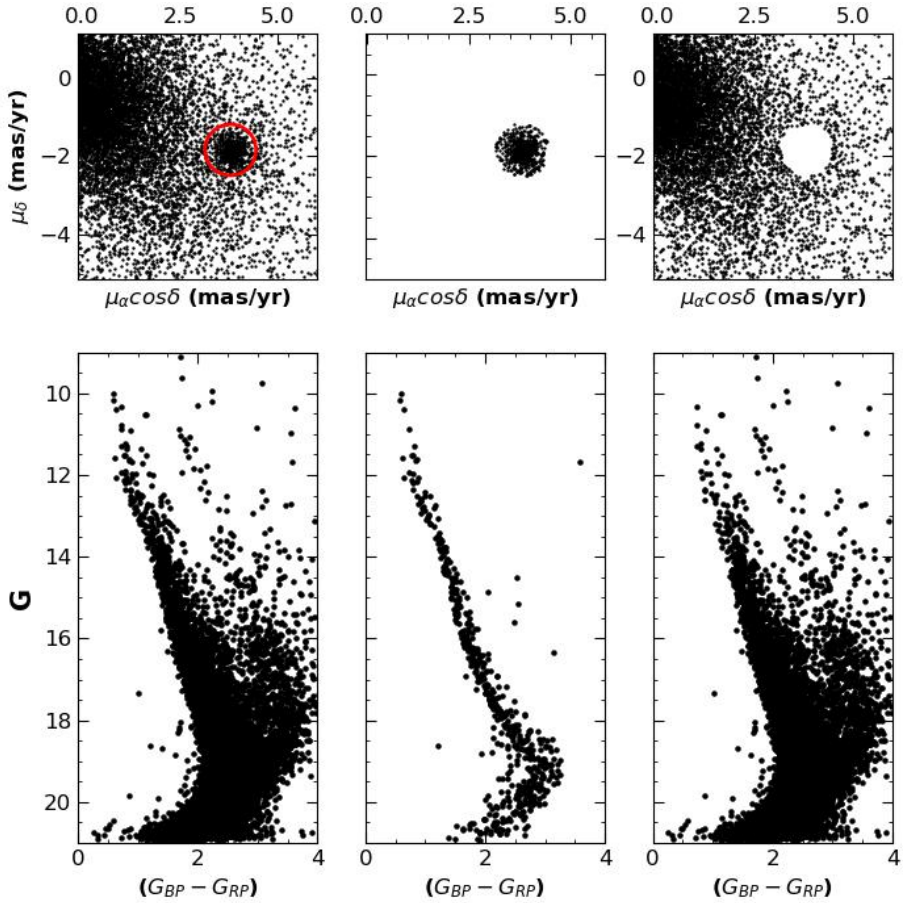

Figure 7. Initial cluster member separation using proper motion. Top panels show the VPDs and bottom panels show the respective CMDs for total, cluster and field region.

The unprecedented astrometric precision of the Gaia DR3 catalogue has significantly improved the reliability of membership determination based on kinematic data (data related to stellar motion) (Castro-Ginard et al., 2018; Castro-Ginard, A. et al., 2019); (Liu & Pang, 2019). Therefore, we used Gaia DR3 data for our kinematic analysis, member star identification, and cluster distance calculations. Figure 7 illustrates the VPDs constructed using the proper motion of cluster stars in RA and Decr. Here, the cluster stars are separated from the field stars, with the cluster members encircled in red, as shown in the upper panel of the figure, and the cluster members are separated from the field stars, as shown by the CMD in the lower panel of Figure 7. This distinction is possible because cluster stars exhibit a more concentrated proper motion distribution than field stars. The center of the red circle was determined using the maximum density method described by Joshi et al. (2020a).

The estimated value of the center of the cluster proper motion distribution is $(\mu_\alpha \cos\delta,\ \mu_\delta) = 3.82$ mas yr^{-1}, -1.90 mas yr^{-1} for King 6. We identified the stars within the red circle as probable cluster members. We identified 575 probable member stars in the cluster. To quantify the membership of the stars, we calculated the membership probabilities. We estimated the membership probabilities using a statistical approach based on the PMs of stars, as described in previous studies (Sanders, 1971; Michalska, 2019; Pandey et al., 2020).

Assuming a distance of 0.75 kpc and a radial velocity dispersion of 1 km s^{-1} for open clusters (Girard et al., 1989), a dispersion (σ_c) of ∼0.28 mas yr^{-1} in the proper motion of the cluster can be obtained. We calculated $\mu_{xf} = 0.15$ mas yr^{-1}, $\mu_{yf} = -0.74$ mas yr^{-1}, $\sigma_{xf} = 5.76$ mas yr^{-1}, and $\sigma_{yf} = 5.53$ mas yr^{-1} for the field stars. These values were used to construct the frequency distributions of the cluster stars (ϕ_c^ν) and field stars (ϕ_f^ν) using the equation given by Yadav et al. (2013). The membership probability for the i^{th} star is calculated using the following equation:

$$P_\mu(i) = \frac{n_c \times \phi_c^\nu(i)}{n_c \times \phi_c^\nu(i) + n_f \times \phi_f^\nu(i)} \qquad (2)$$

where n_c and n_f are the normalized numbers of probable cluster members and field stars, respectively. We found 606 stars with $P_\mu > 0.80$ for the cluster. In Figure 8, we plot the membership probability against G magnitude. In this figure, we can see the separation between cluster members and field stars toward the brighter part, which supports the effectiveness of this technique on the Gaia data. A high

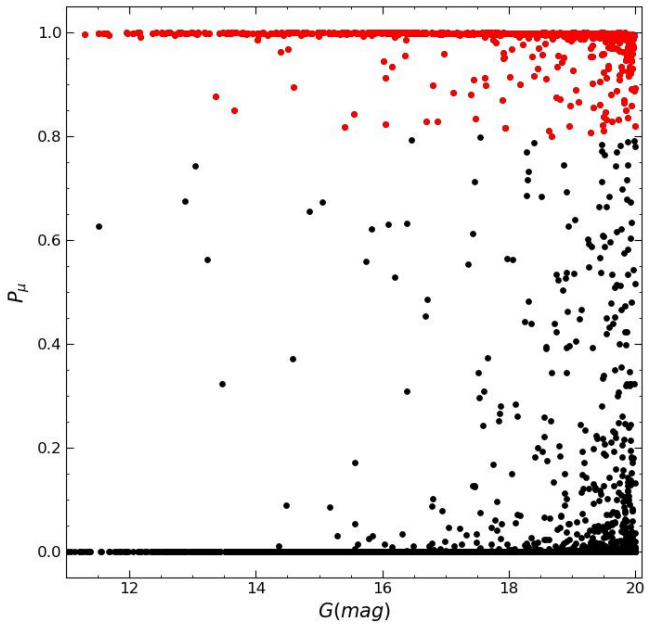

Figure 8. The Gaia membership probability is plotted against G magnitude. The red dot represents the star with a probability of $P_\mu \geq 0.80$, and the black dots represent the star with a probability of $P_\mu < 0.80$.

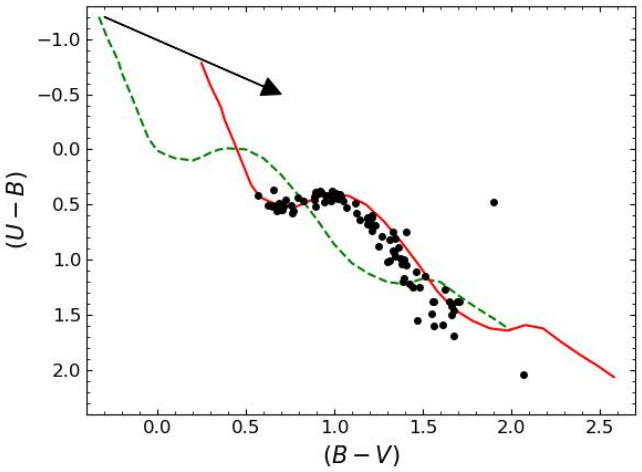

Figure 9. The color-color diagram for target region. The dashed line represents the intrinsic ZAMS, and the solid curve represents the best-fit ZAMS. Arrow illustrates the reddening vector.

membership probability extends to $G \sim 20$ mag, whereas the probability gradually decreases toward fainter limits.

We matched our *UBVRI* catalogue with the Gaia catalogue using a matching radius of 2″.0. We found 242 optical counterparts of Gaia sources with membership probability data. We found 94 stars within the cluster radius (9′) with a membership probability $P_\mu \geq 0.80$.

6. Cluster parameters

6.1. *(U-B)* vs. *(B-V)* diagram

The reddening, $E(B-V)$, can be determined by fitting the intrinsic zero-age main-sequence (ZAMS) on the $(U-B)/(B-V)$ color-color diagram (Phelps & Janes, 1994). The black points denote member stars present within a 9′.0 radius and with probability $P_\mu > 0.80$. The best fit of the intrinsic ZAMS was achieved by shifting $E(B-V)$ along the reddening vector, as shown in Figure 9. We adopted the slope of the reddening vector $E(U-B)/E(B-V) = 0.72$ and fitted the ZAMS with solar metallicity, that is, $Z = 0.02$ (Schmidt-Kaler, 1982). The best fit was achieved for a reddening value of 0.58 ± 0.03 mag. Our estimated value of $E(B-V) = 0.58 \pm 0.03$ mag is comparable to the values estimated by Maciejewski & Niedzielski (2007), Gokmen et al. (2023), and Ann et al. (2002) (see Table 5).

6.2. Total-to selective extinction value

Reddening is an important parameter for star clusters because it can significantly affect the determination of other fundamental parameters. Color-color diagrams are essential for understanding extinction laws. The photons emitted from cluster stars are scattered and absorbed in the interstellar medium by dust particles, leading to a deviation in their color from their intrinsic values. The normal Galactic reddening law may not accurately describe the reddening observed along the line of sight to many star clusters (Sneden et al., 1978). To examine the nature of the reddening law, two color diagrams, $(V-\lambda)/(B-V)$, are employed as suggested by Chini & Wargau (1990), where λ represents all filters other than V. Here, we examined the reddening law for the cluster by drawing two color diagrams, as shown in Figure 10. Because the stellar color values show a linear relationship, a linear equation was applied to calculate the slope ($m_{cluster}$). We calculated the total-to-selective extinction using the relation given by Neckel & Chini (1981),

$$R_{cluster} = \frac{m_{cluster}}{m_{normal}} \times R_{normal} \quad (3)$$

where R_{normal} is the normal value of total-to-selective extinction, taken to be 3.10, and m_{normal} and $m_{cluster}$ are the slopes of a linear fit to two color diagrams for normal extinction and extinction in the direction of clusters, respectively. The values of m_{normal} and $m_{cluster}$ are listed in Table 4. The average $R_{cluster}$ (=2.78 ± 0.30) was approximately equal to the normal value. Thus, the reddening law is normal in the direction of the cluster.

6.3. Distance and Age Determination

A CMD was used to estimate the age and distance of the cluster. V versus $(U-B)$, V versus $(B-V)$, and V versus $(V-I)$ CMDs of the member stars (represented by blue dots) within the cluster radius 9′.0 and $P_\mu \geq 0.80$ are shown in Figure 11. The CMDs of the target cluster show a well-defined, narrow main sequence (MS) locus. The MS extends from $V \sim 11.2-18.8$ mag. The theoretical isochrone of solar metallicity $Z = 0.02$ taken from Bertelli et al. (1994) has been overplotted on the CMDs and is represented by

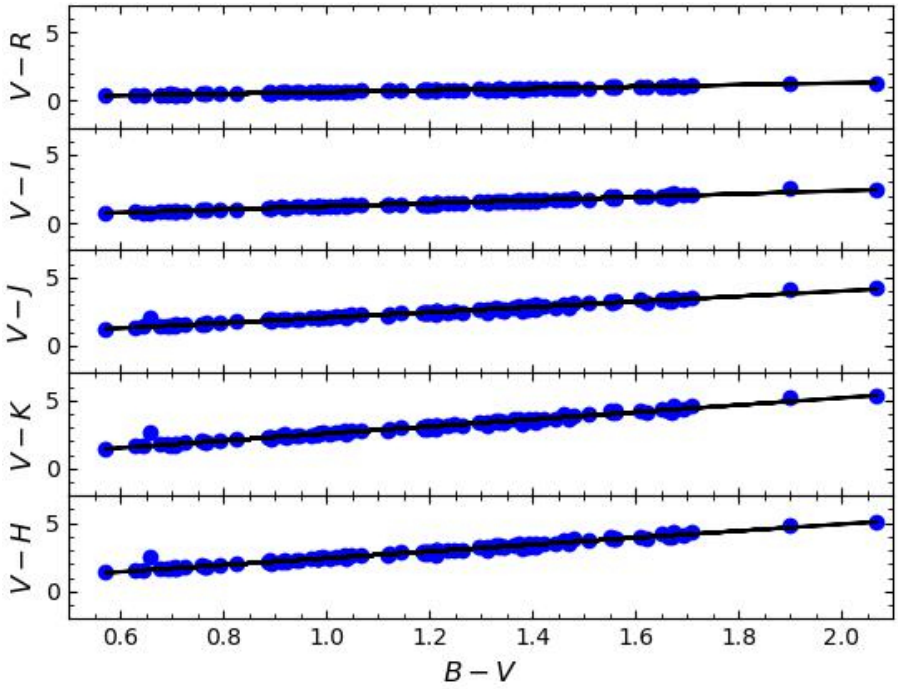

Figure 10. $(V-\lambda)/(B-V)$ color-color diagram is plotted for stars within cluster radius, with membership probability $P_\mu > 0.80$. Continuous line represents the slopes.

Table 4. The slopes of the $(V-\lambda)/(B-V)$ diagrams for the member stars and corresponding normal values

	$\frac{(V-R)}{(B-V)}$	$\frac{(V-I)}{(B-V)}$	$\frac{(V-J)}{(B-V)}$	$\frac{(V-K)}{(B-V)}$	$\frac{(V-H)}{(B-V)}$
Normal	0.80	1.70	2.23	2.72	2.42
King 6	0.66 ± 0.001	1.34 ± 0.001	$1.94 \pm 0..001$	2.61 ± 0.001	2.49 ± 0.001
$R_{cluster}$	2.56	2.44	2.70	2.97	3.19

solid lines. The reddening values derived in Section 6.1 were used for the isochrone-fitting process. The best fit of the theoretical isochrone gives the value of distance modulus as $(V-M_v) = 11.10 \pm 0.40$ mag, giving the distance as 724 ± 5 pc. Our estimated distance value is comparable to those derived by Maciejewski & Niedzielski (2007) and Gokmen et al. (2023) (see Table 5).

We also used the parallax of the stars to obtain the distance to the cluster. In Figure 12, we plot the histogram of the 0.10 mas parallax bin using the star within the cluster radius with the probability membership $P_\mu \geq 0.80$. A Gaussian function was fitted to the histogram. We found a mean parallax of 1.36 ± 0.10 mas. Using this mean parallax, we estimated the distance to be 735 ± 10 pc, which closely agrees with the value derived using the CMDs.

The age of the cluster was determined by fitting theoretical stellar evolutionary isochrones of different ages to the CMDs ($V/(U-B)$, $V/(B-V)$, and $V/(V-I)$). Isochrone fitting was performed considering the bluest envelope of the CMDs, as shown in Figure 11. After correcting for reddening, the best fit was obtained for an age of log(age) = 8.40 ($\sim$ 251 Myr), which is in good agreement with the previously estimated values by Ann et al. (2002), Gokmen et al. (2023), and Maciejewski & Niedzielski (2007), listed in Table 5.

7. Interstellar extinction in near-IR

7.1. *(V-K)* vs. *(J-K)* diagram

We combined *2MASS* JHK_s data with optical data to determine the interstellar extinction in the near-IR. The K_s magnitude was converted into K magnitude using the methods given by Persson et al. (1998). The $(J-K)$ versus $(V-K)$ color-color diagram for the cluster members is shown in the left panel of Figure 13. The solid line in the figure shows the ZAMS given by Bertelli et al. (1994). This ZAMS provides $E(J-K) = 0.24 \pm 0.03$ mag and $E(V-K) = 1.50 \pm 0.01$ mag for the cluster, respectively. The ratio $\frac{E(J-K)}{E(V-K)}$ is $\sim 0.16 \pm 0.03$, which is in good agreement with the normal interstellar extinction value of 0.19 given by Cardelli et al. (1989). This scatter is due to the large error in the JHK data points.

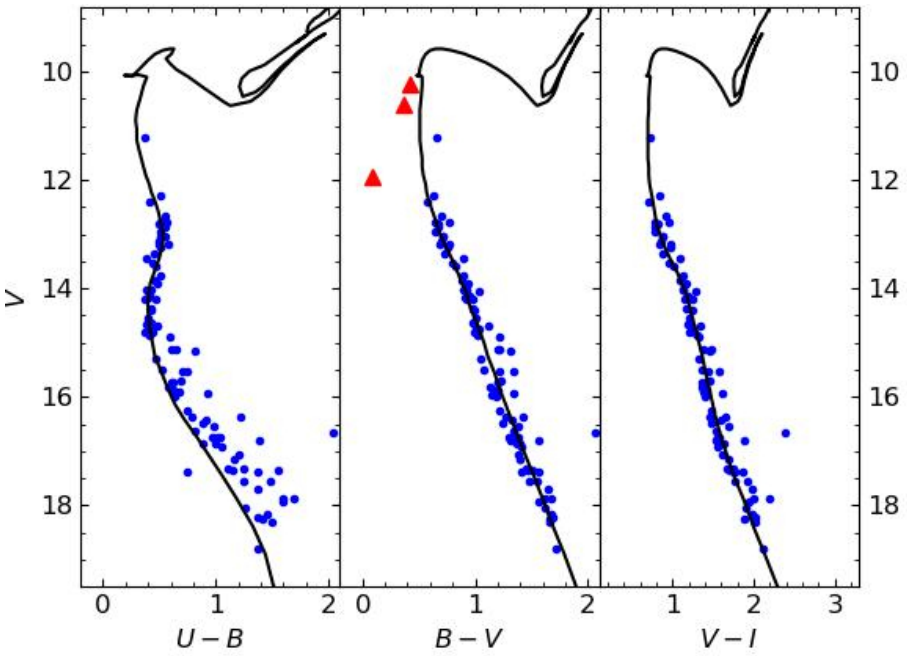

Figure 11. The color-magnitude diagrams for the member stars of the cluster with $P_\mu \geq 0.80$. The red triangles represent positions of variable stars using data from Stassun et al. (2019).

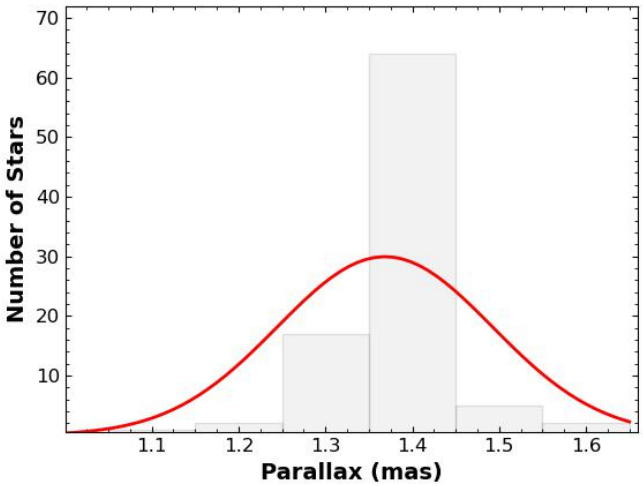

Figure 12. Histogram in parallax (0.10 mas bins) for the cluster region. Red curve represents the Gaussian function fitting.

7.2. *(B-V)* vs. *(J-K)* diagram

We have plotted $(B-V)$ versus $(J-K)$ color-color diagram for the cluster, as shown in the middle panel of Figure 13. We used the ZAMS given by Bertelli et al. (1994) to determine the relationship between the two color indices. The color excesses $E(B-V)$ and $E(J-K)$ were found to be 0.58 and 0.24 mag, respectively. This results in a ratio of $\frac{E(B-V)}{E(J-K)} \sim 0.43$ mag, which is slightly lower than the value of 0.56 reported by Cardelli et al. (1989).

7.3. *(J-H)* vs. *(J-K)* diagram

The $(J-H)$ vs $(J-K)$ color-color diagram for the cluster is shown in the right panel of Figure 13. To determine the relationship between these two colors, we utilized the ZAMS given by Bertelli et al. (1994), as indicated by the solid line in the right panel of figure. We have found that $E(J-H) = 0.15 \pm 0.02$ and $E(J-K) = 0.24 \pm 0.03$. We calculated the value of the ratio $\frac{E(J-H)}{E(J-K)} = 0.64 \pm 0.06$, which is in agreement within 2σ of the normal value of 0.55, as given by Cardelli et al. (1989).

7.4. Age and distance of the cluster using *2MASS* data

Using 2MASS data, we re-determined the cluster distance and age. We have plotted V versus $(V-K)$ in the left panel, J versus $(J-H)$ in the middle panel, and K versus $(J-K)$ in the right panel of Figure 14. We used the theoretical isochrone given by Bertelli et al. (1994) for $Z = 0.02$ of log(age) = 8.40, which has been overplotted in the CMDs. We found an apparent distance modulus of 11.10 ± 0.08, 9.82 ± 0.08, and 9.57 ± 0.08 mag using the CMDs, as shown in Figure 14. This distance modulus leads to a distance of 733 ± 7 pc. The age and distance of the cluster derived using 2MASS data agree with those derived using optical data.

8. Luminosity and mass function

8.1. Luminosity Function

We examined the brightness distribution of stars within the cluster. To achieve this, we considered stars with a probability $P_\mu \geq 0.80$ and within the cluster radius. We

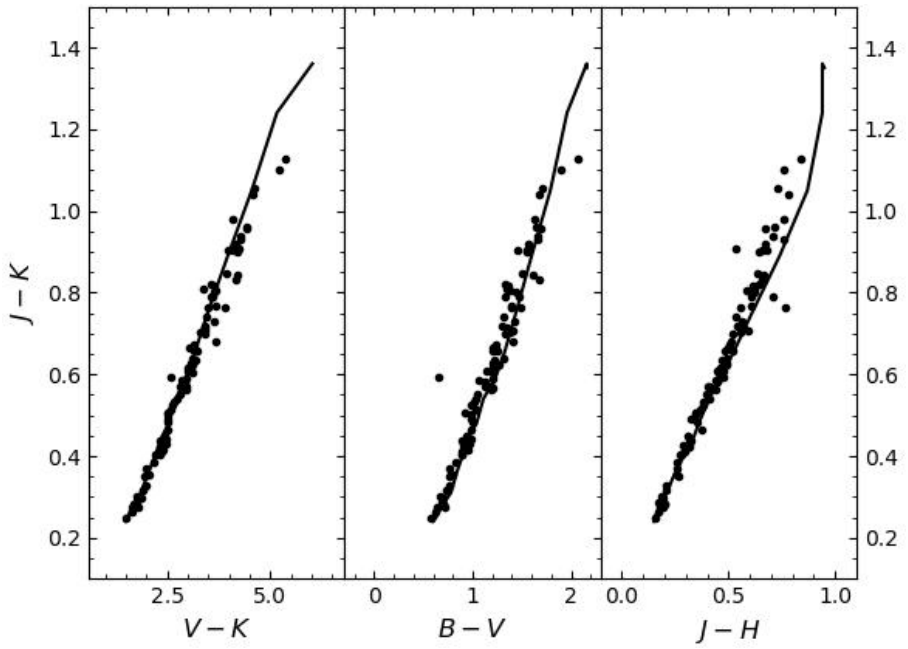

Figure 13. color-color diagram for the stars within the cluster radius and $P_\mu \geq 0.8$. Solid line is the ZAMS taken from Bertelli et al. (1994).

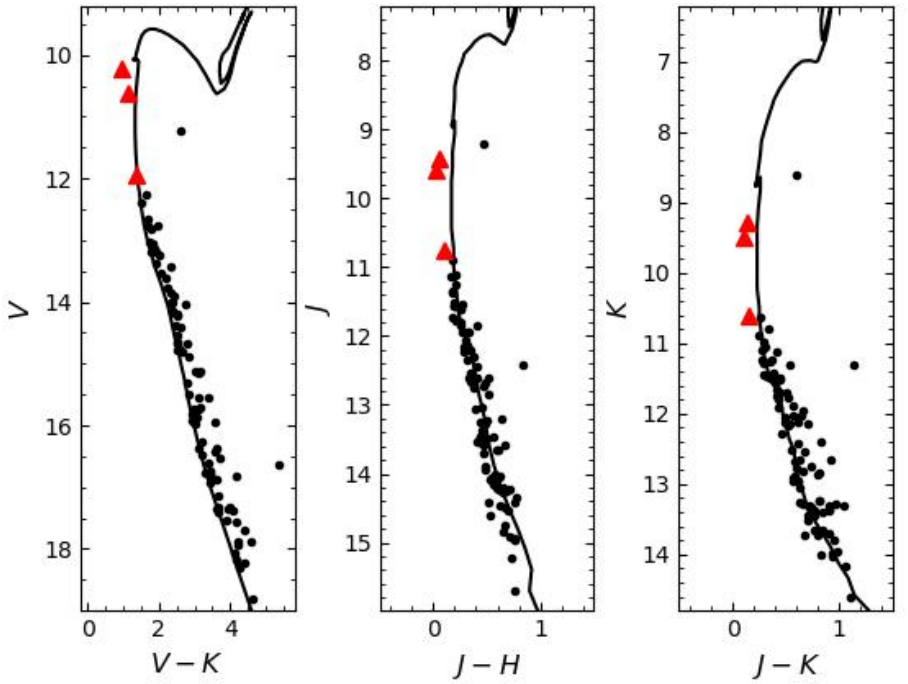

Figure 14. color-magnitude diagram for the stars within cluster radius and $P_\mu \geq 0.80$. Triangular red dots represent the position of variable stars.

considered their apparent brightness (V magnitude) and converted it to their true brightness (absolute magnitude) by accounting for the distance and correction factor (A_V). We grouped stars based on brightness (bins of 1.00 magnitude) to ensure that there were enough stars in each group for a reliable analysis. Finally, by plotting the number of stars in each brightness bin, we created a luminosity function(LF) for the cluster, as shown in Figure 15. Interestingly, this distribution shows an increasing trend up to $M_v \sim 4$ mag and a dip at ~ 5.50 mag for the cluster.

8.2. Mass Function

The mass function (MF), that is, the frequency distribution of stellar masses, is a fundamental parameter for studying

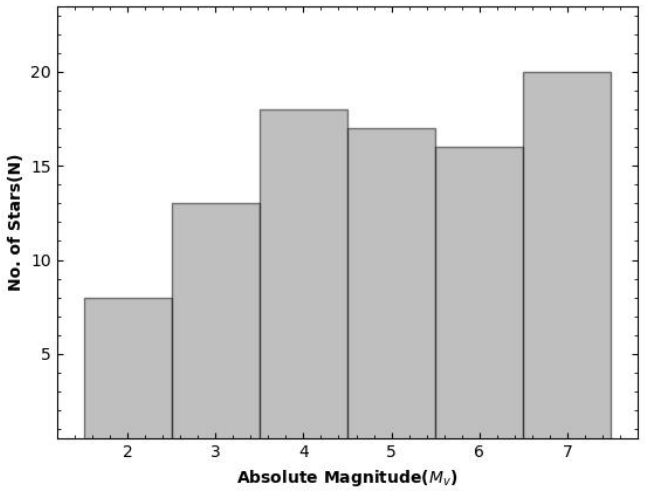

Figure 15. Luminosity function of the cluster region.

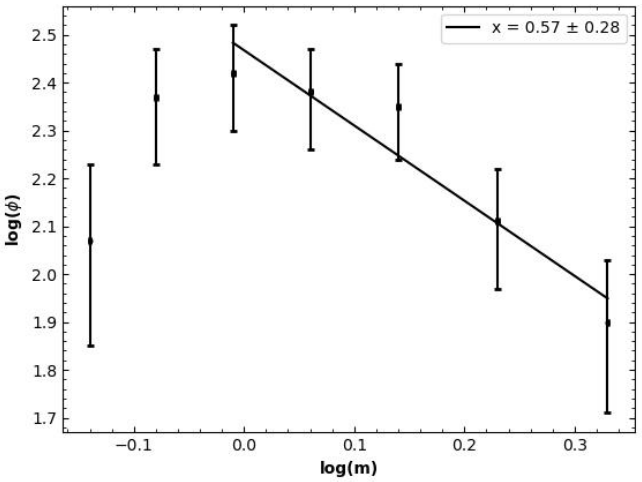

Figure 16. Mass Function for cluster under study derived using Bertelli et al. (1994) isochrone. The error bars represent $\frac{1}{\sqrt{N}}$.

star formation and evolution in clusters. It represents the distribution of stellar masses per unit volume in a star formation event, and knowledge of the MF is very effective in determining the subsequent evolution of the cluster. The MF can be derived using the linear relation

$$\log(dN/dM) = -(1+x) \times \log M + constant \qquad (4)$$

where dN represents the number of stars per mass bin dM with central mass M, and x is the slope of the MF. To convert the LF to the MF, we used the theoretical evolutionary model given by Bertelli et al. (1994), and the resulting MF is shown in Figure 16. This figure shows a turn $\sim 1\,M_{\odot}$. To derive the mass function slope, we considered stars with a mass $\geq 1\,M_{\odot}$. The derived slope of the MF is $x = 0.57 \pm 0.28$, which is less than the value of 1.35 given by Salpeter (1955) for solar neighborhood stars. The calculated mass function slope is less than the mass function slope of 1.29 ± 0.18 determined by Gokmen et al. (2023) within the mass range $0.58 \geq \mathrm{M/M_{\odot}} \geq 3.59$.

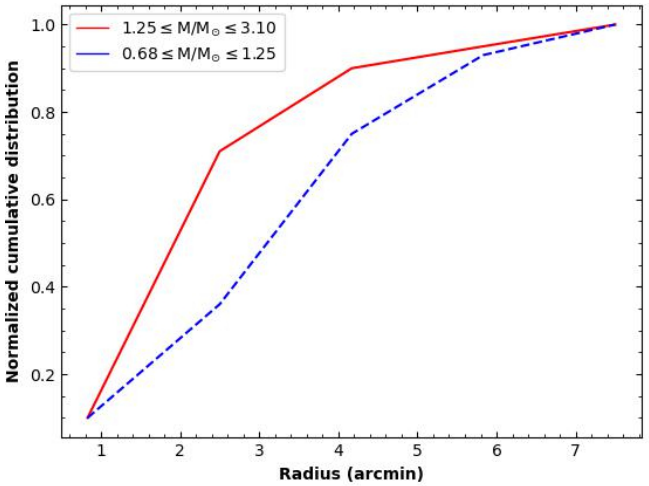

Figure 17. The cumulative radial distribution of member stars in low-mass ($< 1.25M_{\odot}$) and relatively higher-mass ($\geq 1.25M_{\odot}$) range.

9. Mass segregation, relaxation time and tidal radius of the cluster

9.1. Mass segregation

To study the mass segregation of the cluster, we plotted the cumulative radial distribution of the stars for different masses, as shown in Figure 17. To do so, we divided the main-sequence stars into two mass ranges, $3.10 \leq M/M_{\odot} \leq 1.25$ and $1.25 \leq M/M_{\odot} \leq 0.68$ for the cluster. To obtain the mass segregation effect, we selected probable members based on the membership probability and the CMD of the cluster. The figure exhibits the mass segregation effect in the sense that massive stars gradually sink towards the cluster center rather than the fainter stars. To check whether this mass distribution represents the same kind of distribution, we performed the Kolmogorov-Smirnov(K-S) test. This test indicates that the confidence level of the mass segregation effect is 98 % for the cluster.

9.2. The relaxation time

The relaxation time (T_E) is the time scale at which a cluster loses all traces of its initial condition. This is the peculiar time scale for the cluster to reach some extent of energy equipartition. The relaxation time is given by Spitzer Jr & Hart (1971),

$$T_E = \frac{8.9 \times 10^5 (N R_h^3)^{1/2}}{< m >^{1/2} log(0.4N)} \qquad (5)$$

where N is the number of cluster members with probability ($P_{\mu} \geq 0.80$) and within radius $9'.00$, R_h is the half-mass radius of the cluster, and $< m >$ is the mean mass of the cluster stars (Spitzer Jr & Hart, 1971). In our case, the

Table 5. Comparison of our derived fundamental parameters of King 6 with the literature values

Parameters	Numerical Values	Reference
(RA, DEC) (deg)	$(51.98 \pm 0.18, 56.44 \pm 0.10)$	Present study
	51.98, 56.44	(Ann et al., 2002)
$(\mu_\alpha \cos\delta, \mu_\delta)$ (mas yr^{-1})	$(-3.82, -1.90)$	Present study
Cluster Radius (arcmin)	$9'.00$	Present study
	$10'.90$	(Maciejewski & Niedzielski, 2007)
	$10'.00$	(Gokmen et al., 2023)
Cluster Radius(pc)	1.98	Present study
Tidal Radius(pc)	3.18	Present study
ρ_0(stars/arcmin^2)	5.88 ± 0.87	Present tudy
	2.28 ± 0.24	(Gokmen et al., 2023)
r_c(arcmin)	3.58 ± 0.49	Present study
	4.68 ± 1.07	(Gokmen et al., 2023)
ρ_b(stars/arcmin^2)	7.00 ± 0.06	Present study
	5.12 ± 0.16	(Gokmen et al., 2023)
log(age)	8.40	Present study
	8.40 ± 0.10	(Ann et al., 2002)
	8.40	(Maciejewski & Niedzielski, 2007)
	8.58 ± 0.12	(Bossini et al., 2019)
	8.29	(Dias et al., 2021)
	8.30	(Gokmen et al., 2023)
Distance (pc)	724 ± 5	Present study
	426	(Ann et al., 2002)
	800 ± 270	Maciejewski & Niedzielski (2007)
	497	(Bossini et al., 2019)
	704	(Dias et al., 2021)
	723 ± 34	(Gokmen et al., 2023)
$E(B-V)$(mag)	0.58 ± 0.03	Present study
	0.50 ± 0.10	(Ann et al., 2002)
	0.53 ± 0.12	(Maciejewski & Niedzielski, 2007)
	0.34	(Bossini et al., 2019)
	0.59	(Dias et al., 2021)
	0.55 ± 0.03	(Gokmen et al., 2023)
$E(J-K)$(mag)	0.24 ± 0.03	Present study
$E(V-K)$(mag)	1.50 ± 0.01	Present study
$R_{cluster}$	2.78 ± 0.30	Present study
A_v	1.80	Present study
	1.596 ± 0.09	(Gokmen et al., 2023)
Mass function slope (x)	0.57 ± 0.28	Present study
Relaxation Time(Myr)	6.0	Present study

value of $< m >$ was found to be 1 $M_\odot$. The value of R_h is assumed to be half of the radius derived in Section 4. Using the above relation, we estimated the cluster's dynamical relaxation time T_E to be 6.0 Myr. Because the cluster relaxation time is shorter than the cluster age, we conclude that King 6 has dynamically relaxed.

9.3. Tidal radius

The tidal radius of the cluster is the extent to which the gravitational influence of the Galaxy is equal to that of the gravitational influence caused by the cluster core. This can be determined using the following procedure:

The Galactic Mass M_G inside a Galactocentric Radius R_G is given by (Genzel & Townes, 1987)

$$M_G = 2 \times 10^8 M_\odot (\frac{R_G}{30pc})^{1.2} \quad (6)$$

The value of M_G is found to be $1.83{\times}10^{11}$M$_\odot$. Using the formula by Kim et al. (2000), the tidal radius of the cluster

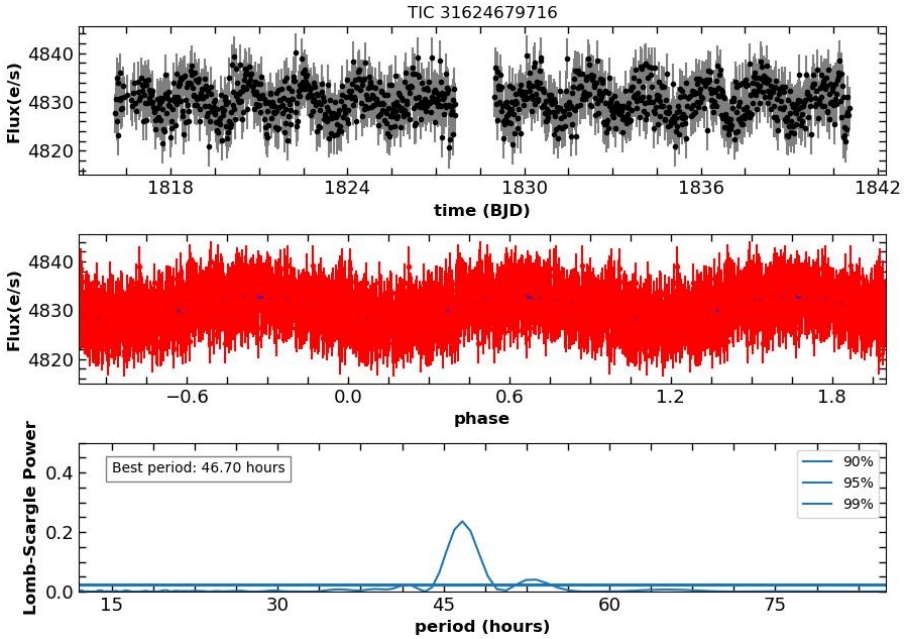

Figure 18. Light curves for the star TIC 31624679716. Upper panel shows light curve, while middle and lower panels show phase-folded light curve and the periodogram.

can be obtained as

$$R_t = (\frac{M_c}{2M_G})^{1/3} \times R_G \quad (7)$$

where R_t and M_c are the tidal radius and total mass of the cluster, respectively. The mass of the cluster was calculated by considering the overall mass function slope derived in this study within the mass range 0.68-3.10$M_\odot$. Thus, the derived tidal radius of the cluster was 3.18 pc. A comparative analysis of the fundamental parameters of King 6, as derived in this study and reported in the literature, is presented in Table 5.

10. Variable stars in the cluster King 6

Variable stars are objects that change their brightness over time. This variation provides critical insights into the physical processes that govern stars. In the present study, we used *TESS* data to search for variable stars in the cluster region. We identified three variable stars (TIC 31624679716, TIC 31632068918, and TIC 3163212399) that were isolated in the SDSS image. The variable stars are plotted in the CMDs shown in Figures 11 and 14. We used the light curve provided by *TESS* to analyze these variables. Their periodicity was determined using the Lomb-scargle algorithm provided by Scargle (1982) and Lomb (1976) for unevenly spaced light curves. The effective temperature (T_{eff}) taken from SIMBAD was 11055, 10510, and 10510 K for TIC 31624679716, TIC 31632068918, and TIC 3163212399, respectively. The temperature values suggest that they are B-type stars. The light curves of each variable are analyzed below.

10.1. TIC 31624679716

The light curve of the star TIC 31624679716 ($RA = 51.8077deg, DEC = 56.3553deg$) is shown in Figure 18. The upper and middle panels show the light and phase-folded light curves, respectively. The light curve exhibited coherent periodic variability. The light curve magnitude change was ~ 0.02 mag. The lower panel shows the Lomb-Scargle periodogram computed from the data in the upper panel. The detected period of the variable star was 46.70 h.

10.2. TIC 31632068918

Figure 19 shows the light curve of the variable star TIC 31632068918 ($RA = 52.0315deg, DEC = 56.3031deg$). The upper and middle panels display the light curve and phase-folded light curve, respectively, while the lower panel shows the Lomb-Scargle periodogram computed from the data presented in the upper panel. The variation in the magnitude was estimated to be ~ 0.01 mag. The derived period of this variable star was 47.92 h.

10.3. TIC 3163212399

The *TESS* light curve of the variable star TIC 3163212399 ($RA = 52.0408deg, DEC = 56.5152deg$) is shown in Figure 20. The upper, middle, and lower panels show the light curve, phase-folded light curve, and Lomb-Scargle periodogram, respectively. A coherent periodicity was observed in the light curve, indicating a magnitude variation of ~ 0.04 mag for the star. The determined period of the star was 37.56 h.

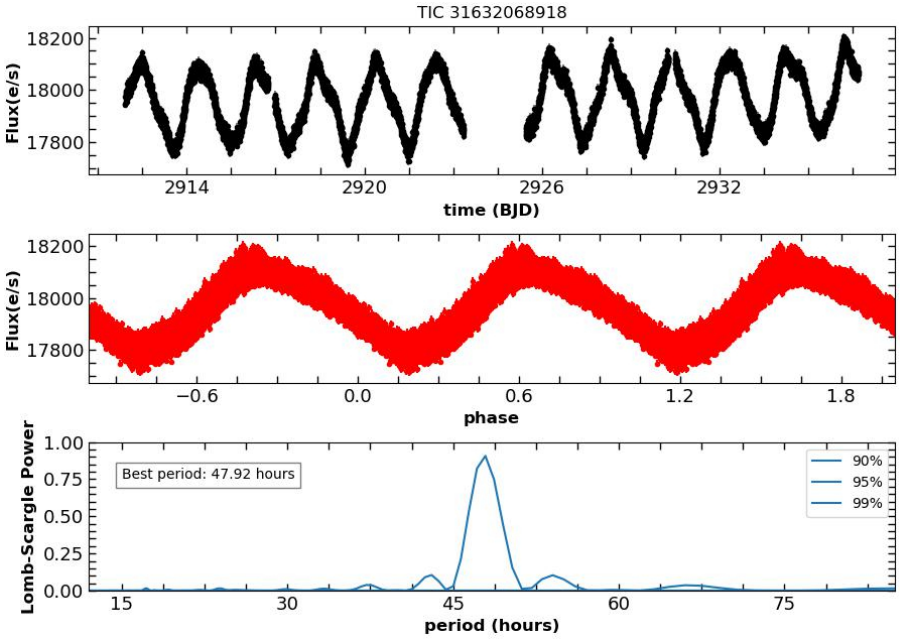

Figure 19. Same as Figure 18 for the variable star TIC 31632068918.

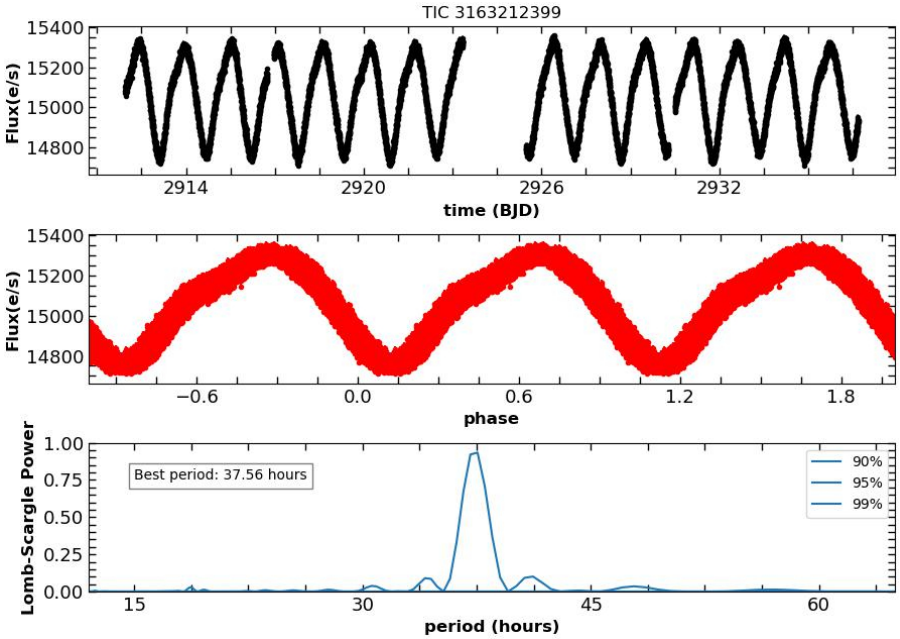

Figure 20. Same as Figure 18 for the variable star TIC 3163212399.

10.4. H-R Diagram and classification of the variables

Variable stars can be classified based on their location on the H-R diagram, shape of their light curves, variability amplitude, and periods. The variable stars searched in this study are plotted in the H-R diagram in Figure 21. The dotted line is the main-sequence curve taken from Pecaut & Mamajek (2013), and the black curve is the region for slow pulsating B-type (SBP) stars (Miglio et al., 2007). Our study identified three variables near the SBP region: the period ranged from 0.30 to 5 days for SPB-type stars, and the magnitude variation was generally less than 0.10 mag. We classified these stars as SPB variables based on their location in the H-R diagram, period, spectral type, magnitude variation, and light curve shape.

11. Conclusion

We have studied the intermediate-age open star cluster King 6 using $UBV(RI)_c$, 2*MASS JHK*, *GAIA* DR3, and *TESS* data. The main findings of this study are as follows:

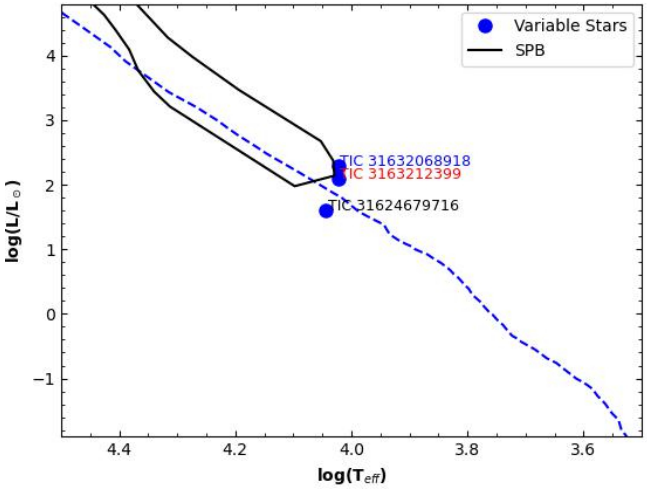

Figure 21. Hertzsprung-Russell ($\log(L/L_\odot)$ vs. $\log(T_{eff})$) diagram for periodic variables within the cluster region.

1. The cluster radius is found to be 9′.0, which corresponds to 1.98 pc at the cluster's distance. The tidal radius of the cluster was determined to be 3.18 pc.
2. From the color-color diagram, we have estimated $E(B-V) = 0.58 \pm 0.03$ for the cluster. The JHK data, in combination with the optical data, provide $E(J-K) = 0.24 \pm 0.03$, and $E(V-K) = 1.50 \pm 0.01$. The value of R_v was 2.78 ± 0.30. Hence, our analysis indicates that the interstellar extinction law is normal in the direction of the cluster.
3. The age of the cluster is found to be 251 Myrs, which is determined using the theoretical isochrone of Bertelli et al. (1994) of solar metallicity $Z = 0.02$.
4. The distance of the cluster is estimated to be 724 ± 5 pc. The distance value is supported by the values determined using near-IR data and the parallax.
5. The luminosity function is determined by considering probable members. We found an increasing trend up to $M_v \sim 4.0$ mag and a dip at ~ 5.50 mag for the cluster. The overall mass function slope is 0.57 ± 0.28, which is less than the Salpeter (1955) value.
6. There is clear evidence of mass segregation within the cluster. The Kolmogorov-Smirnov test indicated a 98% confidence level for this mass segregation. Additionally, the cluster relaxation time was determined to be 6.0 Myr, suggesting that King 6 is dynamically relaxed.
7. We searched variable stars in the cluster region finding three variables with *TESS* ID *TIC* 31624679716, *TIC* 31632068918, and *TIC* 3163212399 for the first time. The variation in the magnitude of the variable stars was 0.02, 0.01, and 0.04 mag, and the period was 46.70, 47.92, and 37.56 h, respectively, classifying them as Slow Pulsating B-type stars.

We are thankful to the anonymous referee for their constructive suggestions on this paper, which significantly improved it. We also acknowledge the use of data from the European Space Agency (ESA) mission Gaia (processed by the Gaia Data Processing and Analysis Consortium, DPAC), which is publicly available from Gaia Data Release 3 (DR3), and the use of data products from the Two-Micron All Sky Survey (*2MASS*), a joint project of the University of Massachusetts and the Infrared Processing and Analysis Center/California Institute of Technology, funded by NASA and the National Science Foundation. This work used data obtained from the Transiting Exoplanet Survey Satellite (*TESS*) mission, which is funded by the NASA Science Mission Directorate. Furthermore, we are grateful to the Aryabhatta Research Institute of Observational Sciences (ARIES) for its support and contributions to this study.

References

Angelo, M. S., Piatti, A. E., Dias, W. S., & Maia, F. F. S. 2019, MNRAS, 488, 1635, doi: 10.1093/mnras/stz1709
Angelo, M. S., Santos, J F C, J., & Corradi, W. J. B. 2020, MNRAS, 493, 3473, doi: 10.1093/mnras/staa517
Ann, H. B., Lee, S. H., Sung, H., et al. 2002, ApJ, 123, 905, doi: 10.1086/338309
Bedding, T. R., Murphy, S. J., Hey, D. R., et al. 2020, Natur, 581, 147, doi: 10.1038/s41586-020-2226-8
Bertelli, G., Bressan, A., Chiosi, C., et al. 1994, A&AS, 106, 275
Bossini, D., Vallenari, A., Bragaglia, A., et al. 2019, A&A, 623, A108, doi: 10.1051/0004-6361/201834693
Cantat-Gaudin, T., Anders, F., Castro-Ginard, A., et al. 2020, A&A, 640, A1, doi: 10.1051/0004-6361/202038192
Cardelli, J. A., Clayton, G. C., & Mathis, J. S. 1989, ApJ, 345, 245, doi: 10.1086/167900
Castro-Ginard, A., Jordi, C., Luri, X., et al. 2018, A&A, 618, A59, doi: 10.1051/0004-6361/201833390
Castro-Ginard, A., Jordi, C., Luri, X., Cantat-Gaudin, T., & Balaguer-Núñez, L. 2019, A&A, 627, A35, doi: 10.1051/0004-6361/201935531
Chini, R., & Wargau, W. F. 1990, A&A, 227, 213
Dias, W. S., Monteiro, H., & Assafin, M. 2018, MNRAS, 478, 5184, doi: 10.1093/mnras/sty1456
Dias, W. S., Monteiro, H., Moitinho, A., et al. 2021, MNRAS, 504, 356, doi: 10.1093/mnras/stab770
Gaia Collaboration, Brown, A. G. A., Vallenari, A., et al. 2016, A&A, 595, A2, doi: 10.1051/0004-6361/201629512
Genzel, R., & Townes, C. H. 1987, ARA&A, 25, 377, doi: 10.1146/annurev.aa.25.090187.002113
Girard, T. M., Grundy, W. M., Lopez, C. E., & van Altena, W. F. 1989, AJ, 98, 227, doi: 10.1086/115139
Gokmen, S., Eker, Z., Yontan, T., et al. 2023, AJ, 166, 263, doi: 10.3847/1538-3881/ad08b0
Higgins, M. E., & Bell, K. J. 2023, AJ, 165, 141, doi: 10.3847/1538-3881/acb20c
Joshi, Y. C., John, A. A., Maurya, J., et al. 2020b, MNRAS, 499, 618, doi: 10.1093/mnras/staa2881

Joshi, Y. C., Maurya, J., John, A. A., et al. 2020a, MNRAS, 492, 3602, doi: 10.1093/mnras/staa029
Kim, S. S., Figer, D. F., Lee, H. M., et al. 2000, ApJ, 545, 301, doi: 10.1086/317807
King, I. 1962, AJ, 67, 471, doi: 10.1086/108756
Lada, C. J., & Lada, E. A. 2003, ARA&A, 41, 57, doi: 10.1146/annurev.astro.41.011802.094844
Landolt, A. U. 1992, AJ, 104, 340, doi: 10.1086/116242
Liu, L., & Pang, X. 2019, ApJS, 245, 32, doi: 10.3847/1538-4365/ab530a
Lomb, N. R. 1976, Ap&SS, 39, 447, doi: 10.1007/BF00648343
Maciejewski, G., & Niedzielski, A. 2007, A&A, 467, 1065, doi: 10.1051/0004-6361:20066588
McKee, C. F., & Ostriker, E. C. 2007, ARA&A, 45, 565, doi: 10.1146/annurev.astro.45.051806.110602
Michalska, G. 2019, MNRAS, 487, 3505, doi: 10.1093/mnras/stz1500
Miglio, A., Montalbán, J., & Dupret, M.-A. 2007, MNRAS, 375, L21, doi: 10.1111/j.1745-3933.2006.00267.x
Neckel, T., & Chini, R. 1981, A&AS, 45, 451
Pandey, R., Sharma, S., Panwar, N., et al. 2020, ApJ, 891, 81, doi: 10.3847/1538-4357/ab6dc7
Pecaut, M. J., & Mamajek, E. E. 2013, ApJS, 208, 9, doi: 10.1088/0067-0049/208/1/9
Persson, S. E., Murphy, D. C., Krzeminski, W., et al. 1998, ApJ, 116, 2475, doi: 10.1086/300607
Phelps, R. L., & Janes, K. A. 1994, ApJS, 90, 31, doi: 10.1086/191857
Piskunov, A., Schilbach, E., Kharchenko, N., et al. 2008, A&A, 477, 165, doi: 10.1051/0004-6361:20078525
Ruprecht, J. 1966, BAICz, 17, 98
Salpeter, E. E. 1955, ApJ, 121, 161, doi: 10.1086/145971
Sanders, W. 1971, A&A, 14, 226
Scargle, J. D. 1982, ApJ, 263, 835, doi: 10.1086/160554
Schmidt-Kaler, T. 1982, 4.1.2 Intrinsic colors and visual absolute magnitudes (calibration of the MK system): Datasheet from Landolt-Börnstein - Group VI Astronomy and Astrophysics · Volume 2B: "Stars and Star Clusters" in SpringerMaterials (https://doi.org/10.1007/10201975_2), Springer-Verlag Berlin Heidelberg, doi: 10.1007/10201975_2
Skrutskie, M., Cutri, R., Stiening, R., et al. 2006, ApJ, 131, 1163, doi: 10.1086/498708
Sneden, C., Gehrz, R. D., Hackwell, J. A., et al. 1978, ApJ, 223, 168, doi: 10.1086/156247
Spitzer Jr, L., & Hart, M. H. 1971, ApJ, 166, 483, doi: 10.1086/150977
Stassun, K. G., Oelkers, R. J., Paegert, M., et al. 2019, AJ, 158, 138, doi: 10.3847/1538-3881/ab3467
Stetson, P. B. 1987, PASP, 99, 191, doi: 10.1086/131977
—. 2000, PASP, 112, 925, doi: 10.1086/316595
Tripathi, A., Panwar, N., Sharma, S., et al. 2023, JApA, 44, 61, doi: 10.1007/s12036-023-09955-7
Trumpler, R. J. 1930, LicOB, 420, 154, doi: 10.5479/ADS/bib/1930LicOB.14.154T
Yadav, R. K. S., Sariya, D. P., & Sagar, R. 2013, MNRAS, 430, 3350, doi: 10.1093/mnras/stt136